PHYSICAL REVIEW APPLIED **17,** 044044 (2022)

Optical Funnel to Guide and Focus Virus Particles for X-Ray Diffractive Imaging

Salah Awel,[1,2] Sebastian Lavin-Varela,[3] Nils Roth,[1,4] Daniel A. Horke,[1,5] Andrei V. Rode,[3,*]
Richard A. Kirian,[6] Jochen Küpper,[1,2,4] and Henry N. Chapman[1,2,4]

[1] *Center for Free-Electron Laser Science, Deutsches Elektronen-Synchrotron (DESY), Notkestrasse 85, Hamburg 22607, Germany*
[2] *Center for Ultrafast Imaging, Universität Hamburg, Luruper Chaussee 149, Hamburg 22761, Germany*
[3] *Laser Physics Centre, Research School of Physics, Australian National University, Canberra ACT 2601, Australia*
[4] *Department of Physics, Universität Hamburg, Luruper Chaussee 149, Hamburg 22761, Germany*
[5] *Radboud University, Institute for Molecules and Materials, Heyendaalseweg 135, Nijmegen 6525 AJ, Netherlands*
[6] *Department of Physics, Arizona State University, Tempe, Arizona 85287, USA*

(Received 14 January 2022; revised 17 March 2022; accepted 22 March 2022; published 22 April 2022)

Photophoretic forces are induced when light causes a net momentum exchange between a particle and a surrounding gas. Such forces have been shown to be a robust means for trapping and guiding particles in air over long distances. Here, we apply the concept of an optical funnel for the delivery of bioparticles to the focus of an x-ray free-electron laser (XFEL) for femtosecond x-ray diffractive imaging. We provide the experimental demonstration of transversely compressing a high-speed beam of aerosolized viruses via photophoretic forces in a low-pressure gas environment. Relative temperature gradients induced on the viruses by the laser are estimated via particle-velocimetry measurements. The results demonstrate the potential for an optical funnel to improve particle-delivery efficiency in XFEL imaging and spectroscopy.

DOI: 10.1103/PhysRevApplied.17.044044

I. INTRODUCTION

X-ray free-electron laser (XFEL) facilities have the potential to enable atomic resolution images of biomolecules at physiological temperatures and with time resolution in the femtosecond regime [1,2]. Since 2009, the serial femtosecond crystallography (SFX) method has yielded nearly 500 protein-structure entries in the protein data bank, many of which are from dynamic systems and are time sequenced with time steps down to 100 fs [3–5]. Single-particle imaging (SPI) aims to extend XFEL imaging to include isolated noncrystallized biomolecules, which would allow the observation of functional molecular motions that may otherwise be hindered in the crystal environment. With the high data-collection rates possible at XFEL facilities [6] combined with the rapid shock-freeze method [7], SPI might enable the detection of rare intermediate states.

The most significant present-day challenge in SPI is the production of high-density nanoparticle beams that can be directed to an x-ray beam of diameter 100–1000 nm in a low-pressure environment [8–12]. Nearly all SPI experiments have utilized aerodynamic focusing injectors for particle delivery [13–15]. Such injectors are well developed and can generate particle beams with diameters on the order of 10 μm [10,12,16,17] but the fraction of x-ray pulses that intercept a biomolecule still remains at less than 0.1 %, for a 100-nm x-ray focus. At this rate, roughly one day of continuous data collection at a 10-kHz detector frame rate would be needed for a full atomic resolution data set consisting of approximately 10^6 diffraction patterns. For these reasons, we consider optical forces as a means to increase the target precision and density of SPI injection systems [18–22].

Previously, we have proposed and investigated an “optical funnel” that uses a focused hollow-core optical vortex beam to guide particles into a tight focus [23,24]. Our design utilizes a laser that counterpropagates against the particle beam to increase the particle density both by slowing the particles as well as by forcing them closer to the beam axis. The inclusion of a surrounding gas activates photophoretic forces, caused by light absorption and subsequent momentum exchange with gas molecules. Photophoretic forces may be larger than optical scattering or gradient forces by orders of magnitude [19,24,25]. The effectiveness of this optical-funnel scheme is complicated by a number of factors, including the optical and thermal properties of the particles, heating and radiation damage, x-ray scattering background caused by the gas, and the three-dimensional profile of the optical beam. While many questions remain, the basic feasibility of the optical-funnel concept has been supported by our preliminary simulation and experimental study, in which photophoretic

---

[*] avr111@physics.anu.edu.au

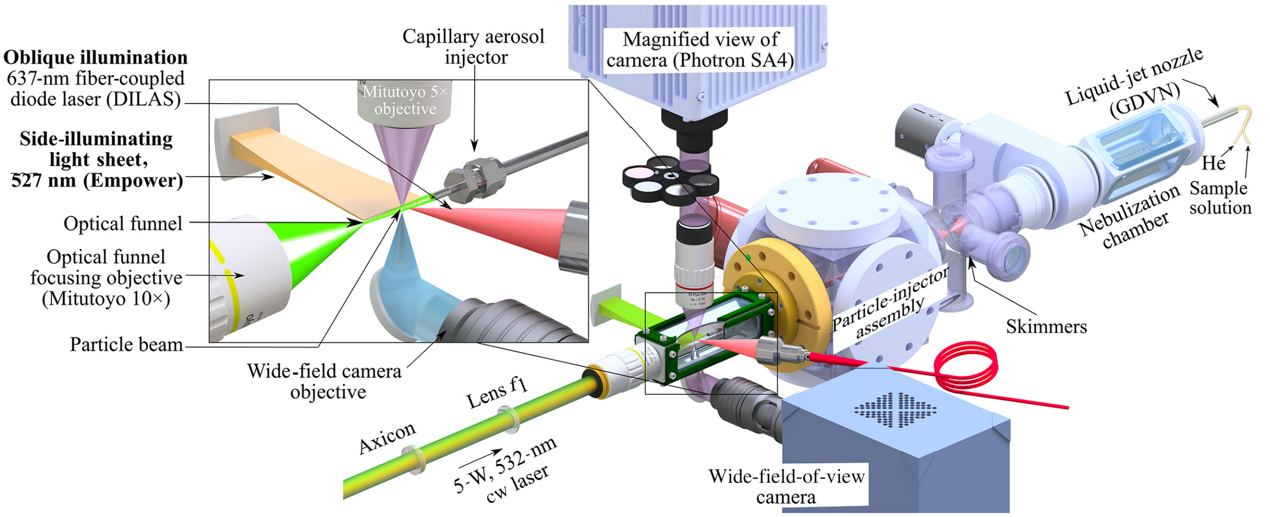

FIG. 1. The basic experimental setup for aerosol particle-beam imaging and focusing.

forces have been directly measured by counterbalancing microparticles against the gravitational force [23,24,26]. Our previous efforts to demonstrate an optical funnel on high-speed particle beams have yielded clear evidence of strong photophoretic forces but no evidence of particle-beam compression, which may have been due to the rapid divergence of the optical beam and limited laser-particle interaction length.

In this paper, we demonstrate particle-beam compression with an optical funnel constructed from a low-divergence hollow-core first-order Bessel beam that extends the particle-laser interaction length by a factor of up to 1000 as compared with a Gaussian beam. The basic experimental setup, shown in Fig. 1, consists of assemblies for optical-funnel beam shaping, aerosolized-particle-beam formation, and high-speed optical imaging.

II. OPTICAL FUNNEL

The optical-funnel profile is achieved by forming a first-order quasi-Bessel beam with a spiral phase plate and an axicon lens and then reimaging the beam inside the chamber with a demagnifying collimator [24,27,28]. The resulting beam changes its size due to the continuously changing magnification along the propagation direction (z axis), as shown in Fig. 2. Since optimization of the optical-funnel geometry for guiding a particular stream of particles is a multiparameter task, we carry out simulations based on Fourier optics [29], modifying the results of Brzobohaty et al. [30] and verifying the results using analytical expressions [31], as discussed in detail in the Supplemental Material [32], Sec. S-I. Figure 2 shows a comparison of the experimental laser-beam profiles along with the numerical simulations [33]. For this comparison, we form an optical funnel with a 532-nm cw Gaussian beam with an output waist $w_0 = 1.4$ mm, which is converted to a first-order Laguerre-Gaussian vortex beam with topological charge $l = 1$ using a 16-step phase plate. The Bessel beam is formed using an axicon with a wedge angle $\alpha_0 = 0.5^\circ$. The beam is reimaged by a demagnifying collimator with $f_1 = 200$ mm and $f_2 = 20$ mm. The formation of this beam is illustrated in Fig. S1 in the Supplemental Material [32]. The resulting optical funnel has a minimum peak-to-peak diameter of 7.5 μm and an angle of divergence in the first bright ring of approximately 1.3×10^{-3} rad.

We direct this optical funnel into a small chamber where we prepare a counterpropagating particle beam in a low-pressure (0.4–0.9 mbar) helium gas environment as shown in Fig. 1. Samples of $265 \times 265 \times 445$ nm^3 *Cydia pomonella* granulovirus capsid particles [34] or 2 μm fluorescent polystyrene spheres are aerosolized with a gas-dynamic virtual nozzle [35,36] at approximately atmospheric pressure and subsequently drawn through a gas nozzle and/or skimmer stage [16,37,38] in order to control the gas pressure. A collimated beam of particles is ejected from a 2-mm-inner-diameter capillary. The particles have speeds in the range of 2–20 m/s, depending on the gas differential pressures. The particle-laser interactions are observed by pulsed-laser Rayleigh-scattering imaging, which localizes the coordinates of individual particles [11,12,16].

III. PARTICLE-BEAM COMPRESSION

A. Particle trajectories

Figure 3(a) shows raw Rayleigh-scattering images of granulovirus particles exposed to a 0.5-W optical funnel at 0.99-mbar pressure. The particles are illuminated by 637-nm 100-ns laser flashes repeating at 25 kHz and

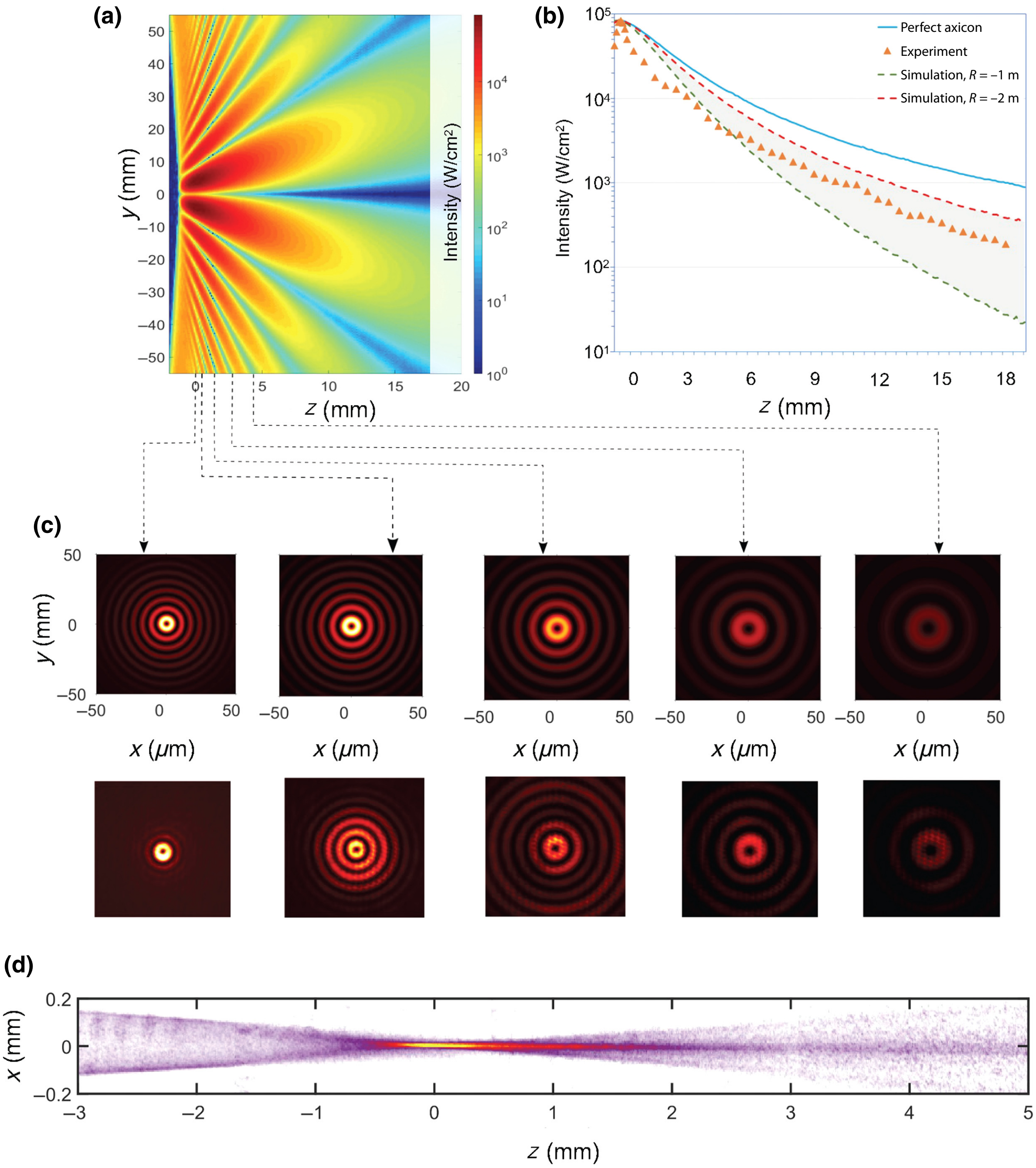

FIG. 2. The slow-diverging optical funnel formed by demagnifying a quasi-Bessel beam with a Keplerian collimator. (a) The simulated optical funnel: the distances are from the maximum-intensity position. (b) A comparison between the experimental intensity profile and a calculated profile in the first ring of the funnel at a total laser power of 1 W. The solid line describes a perfect axicon, whereas the shaded area between the dashed lines indicates the intensity profiles for imperfect axicons with a radius of curvature within the range from 1 m to 2 m of the front face on the axicon. (c) Beam profiles at various cross sections of the optical funnel: the top row shows simulation results, while the bottom row displays the measured profiles. (d) The optical-funnel profile generated by time integrating air scattering in the beam path. The laser beam propagates from left to right toward the particle nozzle.

the scattered light is imaged by a camera. Stroboscopic exposures of the same particle appear in one camera frame, which allows us to calculate the velocities and accelerations from the particle centroid positions [39], as shown in Figs. 3(b)–3(e). The optical beam propagates in the $+z$ direction. Based on the observed accelerations of $2-10\times10^3$ m/s^2 in Figs. 3(b)–3(e), along with an estimated granulovirus mass of 2.2×10^{-14} g calculated

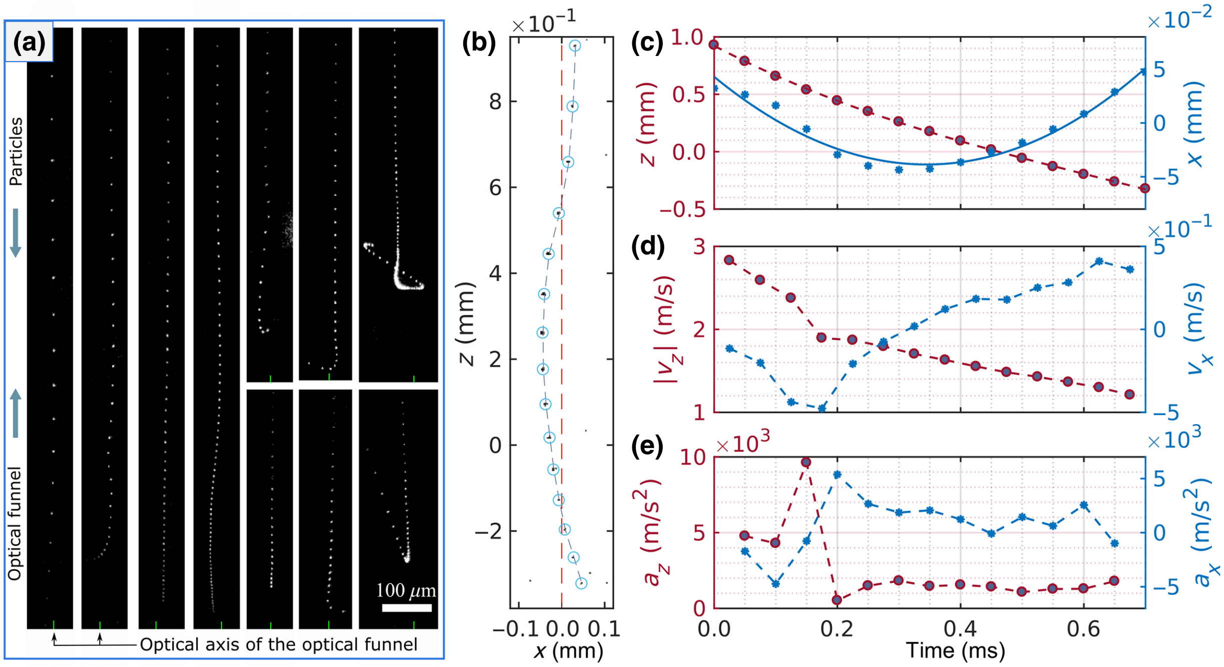

FIG. 3. Granulovirus trajectories recorded with 25-kHz illumination and 0.99-mbar chamber gas pressure. (a) Background-corrected raw images showing particle trajectories in a 2.0-W optical funnel. (b) Centroid positions of a single granulovirus particle trajectory in a 0.5-W optical funnel. The optical axis of the optical funnel is indicated by the dashed red line. (c) Calculated x (blue) and z (red) positions, velocities, and accelerations based on particle centroids in (b).

from the GV density 1.4 g/cm^3 [40], we estimate forces of 0.044–0.22 pN. Particle trajectories in which the viruses dramatically change direction [as seen in Fig. 3(a)] are never observed in the absence of the optical funnel.

Figure 4(a) shows particle-density maps formed from Rayleigh-scattering images with 527-nm-illumination laser flashes reduced to 1 kHz to avoid overlapping particle images. Figure 4(a) shows the effect of a 0.5-W optical funnel on the granulovirus particle beam at 0.4 mbar pressure. The top and bottom density maps compare the densities when the laser is off and on, respectively, while Fig. 4(b) shows plots of the transverse profiles of the particle beams averaged over the $z = 0.5 \pm 0.1$ mm region. Lorentzian fits to these profiles show that the optical funnel induces an approximately threefold increase in peak particle density, while the particle-beam full width at half maximum (FWHM) reduces by a factor of 2. Figure 4(c) shows density maps of 2-μm-diameter polystyrene particle beams at 0.5 mbar chamber pressure, at laser powers of 0 W, 2.5 W, and 5.0 W. The focus of the optical funnel is located at the position $x = z = 0$, outside the field of view of the images. The radial profiles of the particle beams, averaged over $z = [2.4, 2.6]$ mm, are plotted in Fig. 4(d). The Lorentzian fits show that the optical funnel causes the peak particle densities to increase by factors of approximately 3 and 5 for 2.5 W and 5 W laser powers, respectively. Further details on the measurement conditions are listed in Fig. S4 and Table S1 in the Supplementary Material [32].

In our observations, laser powers of 0.5 W and above result in obvious changes to the particle trajectories. The particle-beam compression effect does not confine the particles to the dark 7.5-μm core of the optical funnel as desired; the particle-beam density increases within a broader approximately 150-μm-diameter region, which may be due to the similarly broad initial beam. This could be improved by better matching the phase-space emittance of the particle beam and the acceptance of the optical funnel [7,17]. Along with the transverse compression effect, we also observe increases in the particle-beam density at progressively larger z values (closer to the nozzle) as the laser power is increased. Figure 5 shows the transverse (x) profiles of polystyrene particle-beam densities at $z = 5.5$ mm from the optical-funnel focus for five different laser powers, along with corresponding profiles for a range of z values between 5.2 mm and 7.2 mm. The observed z dependence of the particle density suggests that significant particle-laser interactions begin before particles reach the laser focus. As the particles slow down, they interact with the laser beam for longer durations and with sufficient laser power the particles begin to stop completely and reverse direction, as shown in Fig. S4 in the Supplemental Material [32].

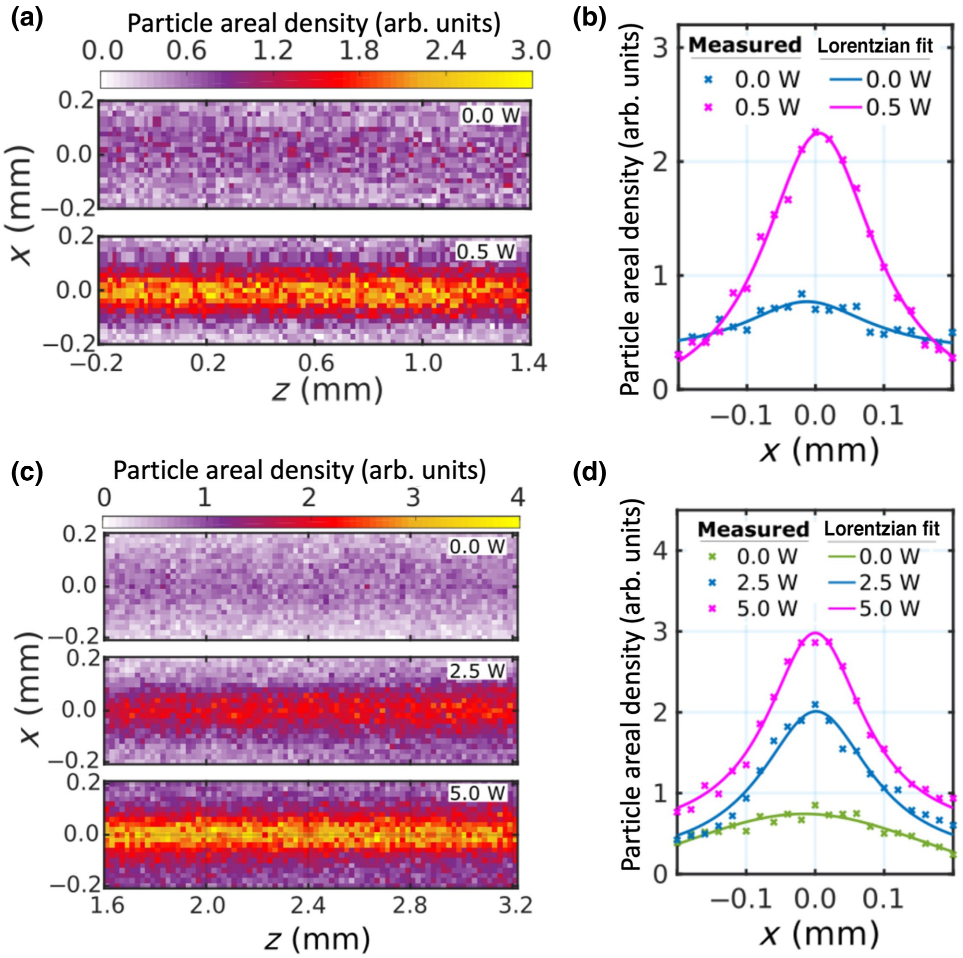

FIG. 4. The focusing of granulovirus particles at 0.4-mbar chamber pressure and 2-μm-diameter polystyrene particles at 0.5-mbar chamber pressure. (a) Granulovirus particle areal-density maps with the laser off (top) and in the presence of a 0.5-W optical funnel (bottom). (b) The 2-μm-diameter polystyrene particle areal-density maps with the laser off (top) and in the presence of 2.5-W (middle) and 5.0-W (bottom) optical-funnel illumination, respectively. The density maps in (a) and (b) are normalized to the peak density in the respective laser-off conditions. (c) The Lorentzian fit to the areal particle densities in (a), averaged over the $z = [0.4, 0.6]$ mm region. (d) The Lorentzian fit to the areal particle density in (b), averaged over the $z = [2.4, 2.6]$ mm region.

B. Temperature gradient

Based on our measured velocities and accelerations, we can estimate the relative temperature gradient $\Delta T/T$ across the particles. Since our measurements are made in the free molecular flow regime, the photophoretic force may be derived from gas-kinetic theory [25,41] and described by the equation

$$F^{\text{pp}} = \frac{\pi}{6}\alpha P r^2 \frac{\Delta T}{T}, \tag{1}$$

where $r \approx 162$ nm is the effective radius of a granulovirus particle, P is the gas pressure, and $\alpha \approx 1$ is the thermal-accommodation coefficient. The observed accelerations are dominated by three forces: the photophoretic force ($\vec{F}^{\text{pp}}$), optical scattering and absorption forces ($\vec{F}^{\text{opt}}$), and the gas drag force ($\vec{F}^{d}$) [42]. As described in Sec. S-VII of the Supplemental Material [32], we determine the velocity-dependent drag force empirically by fitting a line to the equation $a = bv + c$ for our observed accelerations (a) and velocities (v) with the laser turned off. Under the conditions shown in Fig. 4, the values of the coefficients are $b = -810\ \text{s}^{-1}$ and $c = 43\ \text{m/s}^2$. We expect the optical forces to be much lower than the maximum value of $F_z^{\text{opt}} \approx \pi r^2 I/c \approx 8.3 \times 10^{-14}$ N, which corresponds to full absorption at the peak intensity in the optical funnel ($I = 3.0 \times 10^8\ \text{W/m}^2$). For the trajectory shown in Figs. 4(b)–4(e), upon subtracting the gas drag force, the combined photophoretic and optical force is 6.2×10^{-14} N, which suggests that the photophoretic force is indeed dominant, as also suggested by the fact that such curved trajectories do not occur when the laser is turned off. The peak acceleration corresponds to a relative temperature gradient of $\Delta T/T = 0.045$ and $\Delta T \gtrsim 13$ K since $T \gtrsim 298$ K.

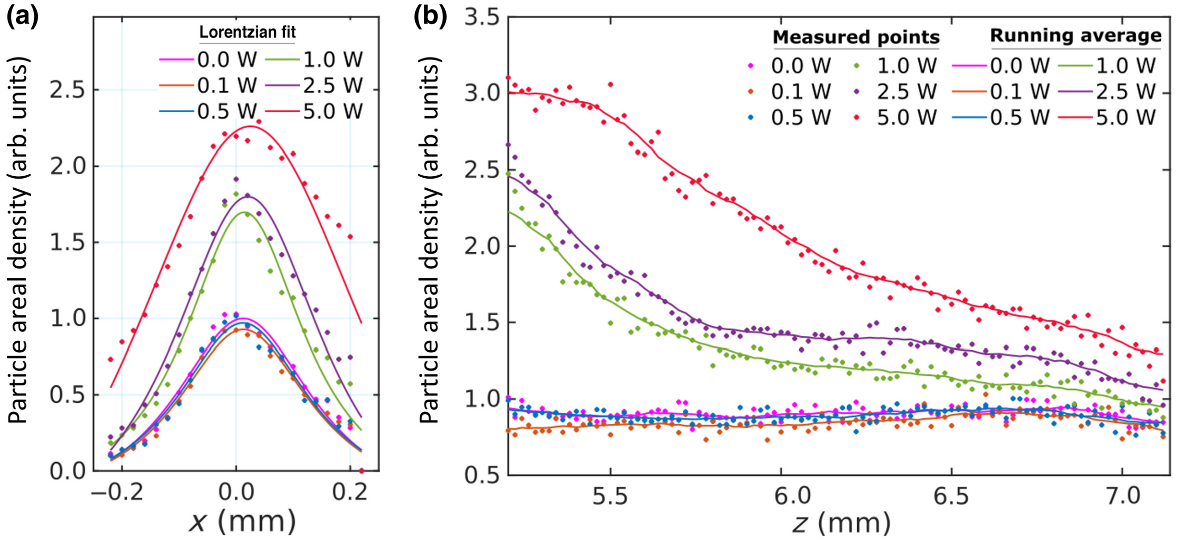

FIG. 5. The increase of the 2-μm-diameter polystyrene particle number density at distances between 5.2 mm and 7.2 mm before the optical-funnel focus, for laser powers between 0 W and 5 W. (a) The radial cross section of the particle-beam density at $z = 5.5$ mm from the optical-funnel focus. (b) The axial cross section along the axis of the particle beams. These number densities are normalized against the peak density with the laser off. The solid line represents the running average calculated over 12 successive points.

If we assume the thermal conductivity g of granulovirus to be approximately the same as most polymers and protein-based materials, $g = 0.3\ \mathrm{W/(m\,K)}$, then the intensity of heat transfer across the granulovirus at this temperature difference is of order $I_{\mathrm{heat}} \approx g\Delta T/r \approx 2.47 \times 10^{7}\ \mathrm{W/m^{2}}$, which is well below the typical threshold for radiation damage.

IV. CONCLUSIONS

In summary, our observations show clear evidence for the focusing of virus particles in a beam due to the photophoretic force in a low-pressure helium gas in the molecular-flow regime. We show that the density of the virus beam can be increased by a factor of 3 when turning on the optical funnel, which will proportionately reduce the measurement time and the amount of sample needed to perform x-ray diffraction measurements. The exact effects of the optical funnel are complicated by the nonlinear dynamics, which are sensitive to the initial particle-beam phase-space density, the surrounding gas pressure and gas velocity, the optical-funnel beam profile, and the precision of the alignment of the optical axis to the particle-beam axis. While it is clear that more detailed calculations and experiments are needed in order to fully understand and optimize an optical-funnel system, the results presented here clearly encourage further research. Based on acceleration measurements, we estimate the relative temperature gradient across the viruses, which is critical to understand as overheating of biological targets is a concern. However, future work that combines an optical funnel with cold particle beams would help avoid the potential of overheating while simultaneously enhancing the magnitude of photophoretic force and greatly improving the aerodynamic focusing, especially when smaller particles are used [7].

ACKNOWLEDGMENTS

We acknowledge support by the Deutsches Elektronen-Synchrotron (DESY), a member of the Helmholtz Association (HGF), and the use of the Maxwell computational resources operated at DESY. This work has been supported by the Deutsche Forschungsgemeinschaft (DFG) through the Clusters of Excellence “Center for Ultrafast Imaging” (CUI, EXC 1074, Grant No. ID 194651731) and “Advanced Imaging of Matter” (AIM, EXC 2056, Grant No. ID 390715994), and by the European Research Council under the European Union’s Seventh Framework Programme (Grant No. FP7/2007-2013) through the Consolidator Grant COMOTION (Grant No. 614507) and by the Australian Research Council’s Discovery Projects funding scheme (Grant No. DP170100131). R.A.K. acknowledges support from the National Science Foundation (NSF) Biology with X-Ray Free Electron Lasers (BioXFEL) Science and Technology Center (STC) award under Grant No. 1231306 as well as NSF Biological Sciences (BIO) Division awards under Grants No. 1943448 and No. 1817862.

S.A., R.A.K., D.A.H., A.V.R., J.K., and H.N.C. conceived the idea and designed the experiment. S.A., D.A.H., N.R., R.A.K., and A.V.R. performed the measurements. S.A. and R.A.K. developed the particle data-analysis tool and analyzed the data. S.L.V. and A.V.R. performed the

optical beam modeling. S.A. wrote the initial version of the manuscript with inputs from R.A.K., S.L.V., and A.V.R. All authors contributed in scientific discussions and manuscript revisions.

The authors declare no competing interests.

[1] R. Neutze, R. Wouts, D. van der Spoel, E. Weckert, and J. Hajdu, Potential for biomolecular imaging with femtosecond X-ray pulses, Nature **406**, 752 (2000).

[2] H. N. Chapman *et al.*, Femtosecond x-ray protein nanocrystallography, Nature **470**, 73 (2011).

[3] H. N. Chapman, X-ray free-electron lasers for the structure and dynamics of macromolecules, Annu. Rev. Biochem. **88**, 35 (2019).

[4] J. C. H. Spence, XFELs for structure and dynamics in biology, IUCrJ **4**, 322 (2017).

[5] I. Schlichting, Serial femtosecond crystallography: The first five years, IUCrJ **2**, 246 (2015).

[6] K. Ayyer *et al.*, 3D diffractive imaging of nanoparticle ensembles using an x-ray laser, Optica **8**, 15 (2021).

[7] A. K. Samanta, M. Amin, A. D. Estillore, N. Roth, L. Worbs, D. A. Horke, and J. Küpper, Controlled beams of shock-frozen, isolated, biological and artificial nanoparticles, Struct. Dyn. **7**, 024304 (2020).

[8] M. J. Bogan, W. H. Benner, S. Boutet, U. Rohner, M. Frank, A. Barty, M. M. Seibert, F. Maia, S. Marchesini, S. Bajt, B. Woods, V. Riot, S. P. Hau-Riege, M. Svenda, E. Marklund, E. Spiller, J. Hajdu, and H. N. Chapman, Single particle x-ray diffractive imaging, Nano Lett. **8**, 310 (2008).

[9] J. Bielecki *et al.*, Electrospray sample injection for single-particle imaging with x-ray lasers, Sci. Adv. **5**, eaav8801 (2019).

[10] N. Roth, S. Awel, D. A. Horke, and J. Küpper, Optimizing aerodynamic lenses for single-particle imaging, J. Aerosol Sci. **124**, 17 (2018).

[11] S. Awel, R. A. Kirian, N. Eckerskorn, M. Wiedorn, D. A. Horke, A. V. Rode, J. Küpper, and H. N. Chapman, Visualizing aerosol-particle injection for diffractive-imaging experiments, Opt. Express **24**, 6507 (2016).

[12] R. A. Kirian *et al.*, Simple convergent-nozzle aerosol injector for single-particle diffractive imaging with x-ray free-electron lasers, Struct. Dyn. **2**, 041717 (2015).

[13] W. K. Murphy and G. W. Sears, Production of particulate beams, J. Appl. Phys. **35**, 1986 (1964).

[14] P. Liu, P. J. Ziemann, D. B. Kittelson, and P. H. McMurry, Generating particle beams of controlled dimensions and divergence: I. Theory of particle motion in aerodynamic lenses and nozzle expansions, Aerosol Sci. Techn. **22**, 293 (1995).

[15] P. Liu, P. J. Ziemann, D. B. Kittelson, and P. H. McMurry, Generating particle beams of controlled dimensions and divergence: II. Experimental evaluation of particle motion in aerodynamic lenses and nozzle expansions, Aerosol Sci. Techn. **22**, 314 (1995).

[16] M. F. Hantke, J. Bielecki, O. Kulyk, D. Westphal, D. S. D. Larsson, M. Svenda, H. K. N. Reddy, R. A. Kirian, J. Andreasson, J. Hajdu, and F. R. N. C. Maia, Rayleigh-scattering microscopy for tracking and sizing nanoparticles in focused aerosol beams, IUCrJ **5**, 673 (2018).

[17] L. Worbs, N. Roth, J. Lübke, A. D. Estillore, P. L. Xavier, A. K. Samanta, and J. Küpper, Optimizing the geometry of aerodynamic lens injectors for single-particle coherent diffractive imaging of gold nanoparticles, J. Appl. Crystallogr. **54**, 1730 (2021).

[18] D. McGloin, D. R. Burnham, M. D. Summers, D. Rudd, N. Dewar, and S. Anand, Optical manipulation of airborne particles: Techniques and applications, Faraday Discuss. **137**, 335 (2008).

[19] V. G. Shvedov, A. V. Rode, Y. V. Izdebskaya, A. S. Desyatnikov, W. Krolikowski, and Y. S. Kivshar, Giant Optical Manipulation, Phys. Rev. Lett. **105**, 118103 (2010).

[20] D. R. Burnham and D. McGloin, Modeling of optical traps for aerosols, J. Opt. Soc. Am. B **28**, 2856 (2011).

[21] V. G. Shvedov, A. S. Desyatnikov, A. V. Rode, W. Krolikowski, and Y. S. Kivshar, Optical guiding of absorbing nanoclusters in air, Opt. Express **17**, 5743 (2009).

[22] D. E. Smalley, E. Nygaard, K. Squire, J. V. Wagoner, J. Rasmussen, S. Gneiting, K. Qaderi, J. Goodsell, W. Rogers, M. Lindsey, K. Costner, A. Monk, M. Pearson, B. Haymore, and J. Peatross, A photophoretic-trap volumetric display, Nature **553**, 486 (2018).

[23] N. Eckerskorn, L. Li, R. A. Kirian, J. Küpper, D. P. DePonte, W. Krolikowski, W. M. Lee, H. N. Chapman, and A. V. Rode, Hollow Bessel-like beam as an optical guide for a stream of microscopic particles, Opt. Express **21**, 30492 (2013).

[24] N. Eckerskorn, R. Bowman, R. A. Kirian, S. Awel, M. Wiedorn, J. Küpper, M. J. Padgett, H. N. Chapman, and A. V. Rode, Evaluation of Optically Induced Forces Imposed in an Optical Funnel on a Stream of Particles in Air and in Vacuum, Phys. Rev. Appl. **4**, 064001 (2015).

[25] H. Rohatschek, Semi-empirical model of photophoretic forces for the entire range of pressures, J. Aerosol Sci. **26**, 717 (1995).

[26] W. Zhu, N. Eckerskorn, A. Upadhya, L. Li, A. V. Rode, and W. M. Lee, Dynamic axial control over optically levitating particles in air with an electrically-tunable variable-focus lens, Biomed. Opt. Express **7**, 2902 (2016).

[27] R. W. Bowman and M. J. Padgett, Optical trapping and binding, Rep. Prog. Phys. **76**, 026401 (2013).

[28] J. H. McLeod, The axicon: A new type of optical element, J. Opt. Soc. Am. **44**, 592 (1954).

[29] B. E. Saleh and M. C. Teich, *Fundamentals of Photonics* (Wiley-Interscience, Hoboken, New Jersey, 2007).

[30] O. Brzobohatý, T. Čižmár, and P. Zemánek, High quality quasi-Bessel beam generated by round-tip axicon, Opt. Express **16**, 12688 (2008).

[31] V. Jarutis, R. Paškauskas, and A. Stabinis, Focusing of Laguerre-Gaussian beams by axicon, Opt. Commun. **184**, 105 (2000).

[32] See the Supplemental Material at http://link.aps.org/supplemental/10.1103/PhysRevApplied.17.044044 for Modelling and formation of optical funnel (S-I, S-II); Sample preparation (S-III); Aerosol injection (S-IV); Particle imaging (S-V); Data analysis (S-VI); Estimation of forces and temperature gradients (S-VII); Positioning of the optical funnel

in the camera FOV (S-VIII); and Experimental parameters (S-IX).

[33] S. Lavin-Varela, M. Ploschner, and A. Rode, in *Optical Trapping and Optical Micromanipulation XVI*, edited by K. Dholakia and G. C. Spalding, International Society for Optics and Photonics (SPIE, 2019), Vol. 11083, p. 244.

[34] C. Gati *et al.*, Atomic structure of granulin determined from native nanocrystalline granulovirus using an x-ray free-electron laser, Proc. Natl. Acad. Sci. U.S.A. **114**, 2247 (2017).

[35] D. P. DePonte, U. Weierstall, K. Schmidt, J. Warner, D. Starodub, J. C. H. Spence, and R. B. Doak, Gas dynamic virtual nozzle for generation of microscopic droplet streams, J. Phys. D **41**, 195505 (2008).

[36] K. R. Beyerlein, L. Adriano, M. Heymann, R. Kirian, J. Knoska, F. Wilde, H. N. Chapman, and S. Bajt, Ceramic micro-injection molded nozzles for serial femtosecond crystallography sample delivery, Rev. Sci. Instrum. **86**, 125104 (2015).

[37] D. Oberthür *et al.*, Double-flow focused liquid injector for efficient serial femtosecond crystallography, Sci. Rep. **7**, 44628 (2017).

[38] S. Awel *et al.*, Femtosecond X-ray diffraction from an aerosolized beam of protein nanocrystals, J. Appl. Cryst. **51**, 133 (2018).

[39] M. Ester, H.-P. Kriegel, J. Sander, and X. Xu *et al.*, in *KDD-96: Proceedings of the Second International Conference on Knowledge Discovery and Data Mining* (1996), Vol. 96, p. 226.

[40] M. L. Quillin and B. W. Matthews, Accurate calculation of the density of proteins, Acta Cryst. D **56**, 791 (2000).

[41] H. Horvath, Photophoresis—a forgotten force ??, KONA Powder and Particle Journal **31**, 181 (2014).

[42] D. K. Hutchins, M. H. Harper, and R. L. Felder, Slip correction measurements for solid spherical particles by modulated dynamic light scattering, Aerosol Sci. Techn. **22**, 202 (1995).

Supplemental Materials

Optical funnel to guide and focus virus particles for x-ray diffractive imaging

Salah Awel,[1,2] Sebastian Lavin-Varela,[3] Nils Roth,[1,4] Daniel A. Horke,[1,5]
Andrei V. Rode,[3] Richard A. Kirian,[6] Jochen Küpper,[1,2,4] and Henry N. Chapman[1,2,4]

[1] *Center for Free-Electron Laser Science, Deutsches Elektronen-Synchrotron*
DESY, Notkestrasse 85, 22607 Hamburg, Germany
[2] *Center for Ultrafast Imaging, Universität Hamburg,*
Luruper Chaussee 149, 22761 Hamburg, Germany
[3] *Laser Physics Centre, Research School of Physics, Australian*
National University, Canberra, ACT 2601, Australia
[4] *Department of Physics, Universität Hamburg,*
Luruper Chaussee 149, 22761 Hamburg, Germany
[5] *Radboud University, Institute for Molecules and Materials,*
Heyendaalseweg 135 , 6525 AJ Nijmegen, Netherlands
[6] *Department of Physics, Arizona State University, Tempe, AZ 85287, USA*

(Dated: 2022-04-05)

S-I. MODELLING OF OPTICAL FUNNEL

Our numerical optical funnel simulation is based on a free-space propagation method using Fourier optics with phase shifts caused by the optical elements [1]. The numerical simulations start with the description of the Gaussian beam. The complex amplitude U_g of the beam is given, in cylindrical coordinates, by:

$$U_g(r, z = 0) = \left(2\frac{P_{tot}}{\pi w_0^2}\right)^{1/2} \exp\left(-\frac{r^2}{w_0^2}\right), \tag{S.1}$$

where w_0 and P_{tot} are the waist and the total power of the initial Gaussian beam, respectively, and $r = \sqrt{x^2 + y^2}$ is the radial coordinate. The complex-valued field at a particular plane z can be propagated by convolution with the Fresnel propagator or multiplied by the complex representation of the phase modulation of a particular optical element. A full description of the phase modulation induced by each optical element is given below.

A. Phase shift produced by a phase plate

A vortex phase plate is a diffractive element with helical thickness variation that induces a linear phase shifts with respect to the azimuthal angle ϕ. This structure controls the phase of the transmitted beam azimuthally, transforming a Gaussian beam into a Laguerre-Gaussian vortex beam. The resulting field at a distance z_v from the Gaussian beam source will be:

$$U_l(r, \phi, z_v) = U_g(r, z_v)\left(\sqrt{\frac{2}{|l|!}}\frac{r}{w_0}\right)^{|l|} \times \exp\left(-\frac{r^2}{w_0^2} + il\varphi\right) \tag{S.2}$$

where ϕ is the azimuthal coordinate and l is the azimuthal index, respectively.

The index l, also called topological charge, refers to the number of 2π cycles in the helical structure of the phase plate, making an increasing numbers of spiral staircases proportional to the index [2]. The topological charge is responsible for the amount of angular momentum of photons that compound the beam and the size of the hollow core of the vortex beam, both directly proportional to l. We note here that the diameter of the vortex beam ring at maximum intensity, $2w_l$, is related to the waist of the initial Gaussian beam by $w_l = w_0\sqrt{|l|/2}$

.

B. Phase shift produced by an axicon

To imprint the phase shift required to transform an incoming beam into a quasi-Bessel beam, an optical element of a conical shape is used, called an axicon [3]. When the axicon is evenly illuminated, it refracts the incoming plane waves into waves that cover a conical surface with an angle α_0. After passing the axicon the interfering wavefronts create an intensity profile described by several concentric rings, whose distribution depends on the topological charge of the incident beam as well as the axicon geometry and refractive index.

The angle between the optical axis and the normal of the refracted wavefront, β, is given by axicon parameters as

$$\beta = \frac{n - n_0}{n_0}\alpha_0 = \frac{n - n_0}{n_0}\frac{\pi - \tau}{2}. \tag{S.3}$$

for a refractive index n of the axicon and the surrounding medium n_0, and τ is the apex angle of the axicon (Figure S.1 (b)).

In order to compare the experimental results with the simulations we need to take into account the imperfection of the conical surface of the axicon. This was done by introducing a radius of curvature on the front-face of the axicon, which affects the intensity distribution in the propagation of the optical field. To derive an expression for the transmitted field we treat the axicon as a thin optical element. Thereby, we introduced a variable radius of curvature R on the front (ideally plane) face of the axicon to find the optimal match between the simulation and experiment. The expression for the field modulation by the axicon is a modification of Brzobohaty et al.[6] who represented its conical surface as a hyperboloid of revolution of two sheets. The field is written as follows,

$$\begin{aligned} U_{ax}(r, z_{axi}) &= U_l(r, z_{axi}) \exp(ikn\Delta_0) \times \\ &\exp\left\{ ik(n_0 - n)\left[R\left(1 - \sqrt{1 - \frac{r^2}{R}}\right) + \left(a^2 + \frac{r^2}{\tan^2(\tau/2)}\right)^{1/2} \right] \right\} \end{aligned} \tag{S.4}$$

where z_{axi} is the distance from phase plate to the axicon and Δ_0 is the axicon maximum thickness. The field distribution $U_l(r, z_{axi})$ is the result of the free-space propagation over a distance z_{axi} of the field produced by the phase plate $U_l(r, z_v)$ using Equation S.2. The parameter a is of least importance in our case because the vortex beam has a singularity

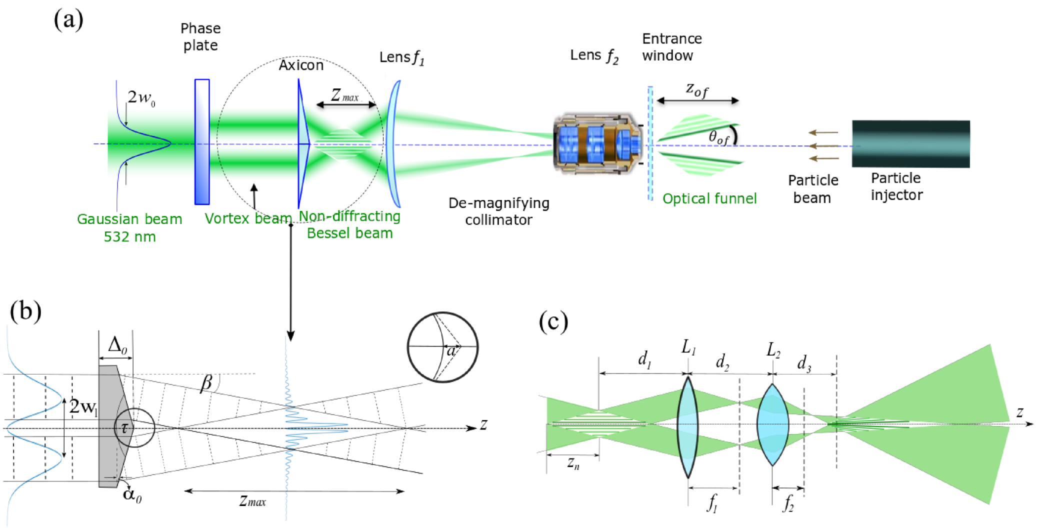

FIG. S.1. (a) Schematic illustration of the optical funnel formation. The initial Gaussian beam is transformed into a hollow-core Laguerre-Gaussian beam by the spiral phase plate. The first-order Bessel beam is formed by the axicon lens. The combined lenses f_1 and f_2 form the de-magnifying collimator that results in the slow-diverging optical funnel due to the varying magnifications of the Bessel beam image [4, 5]. (b) Propagation of a high-order Laguerre-Gaussian beam through an axicon of thickness Δ_0. The plane wavefront is refracted by the axicon, forming a new beam, whose plane waves propagate over a surface of a cone with an angle β. These wavefronts interfere, creating the quasi-Bessel beam within a limited length z_{max}. The round-shaped tip of the axicon (inset) is included into the simulations to achieve an accurate modeling of the experimental interference pattern forming the optical funnel. (c) Constructing the optical funnel by de-magnifying a quasi-Bessel beam with a Keplerian collimator. The distances d_1, d_2, and d_3 are the distance from the object to first lens, the distance between lenses and the distance from the second lens to the image, respectively.

on its axis, which leads to negligible effect due to the minimal interaction with the central region of the axicon. This can be seen when we compare the incident beam, with a waist of several millimetres, to the parameter a, typically in the range of tens of micrometres.

In order to give a fully quantitative description of the Bessel beam axial propagation, it is required to provide an expression for the length and the position of focus of the beam. These expressions can be found in the work of Jarutis at al.[7], where they described the focusing properties of the high-order Bessel beams using an axicon,

$$z_{max} = \frac{0.8 w_0}{\tan\beta} \tag{S.5}$$

$$z_f(l) = \frac{w_0\sqrt{2l+1}}{2\tan\beta}. \tag{S.6}$$

z_{max} in Equation S.5 shows the maximum distance where the interference effect is still active, i.e. the limited volume where the beam is created, while Equation S.6 describes the position of maximum intensity, also called the focus of the Bessel beam. Comparing Equation S.5 and Equation S.6, we note that the focus position of the beam depends on the vortex order, whereas the length does not. This difference is because with the increase of topological charge, the singularity of the vortex is increased, and consequently, the interference starts at a longer distance from the axicon, whereas the region of the interference will not be modified, because the ring width does not change when the index l is modified. Based on this work, we can derive an expression for the core radius of the Bessel beam when $z \gg r$:

$$r_0 = \frac{j_{(l,m)}\lambda}{2\pi\tan(\beta)} \tag{S.7}$$

where $j_{l,m}$ is the m-th maximum of the Bessel function of first kind and l-th order.

C. Phase shift produced by a lens

After the modulation provided by the phase plate and the axicon, the beam enters the re-imaging system. A thin lens with focal length f_i shapes an incoming beam by adding a phase equal to $-ikr^2/(2f_i)$. The resulting field just behind the lens is obtained from:

$$U_{Li}(r, z_{Li}) = U(r, z_{Li}) \exp\left(-i\frac{k}{2f_i}r^2\right) \tag{S.8}$$

The distances z_{Li} denote the position of the i-th lens relative to the previous optical element.

D. Re-imaging of the Bessel beam

Re-imaging is important part of the optical setup as it adds the divergence to the optical funnel and controls the minimum size of the beam and its position on the axis. The de-magnifying collimator is comprised by two thin lenses $L1$ and $L2$, with focal lengths f_1 and f_2. The optical system can be optimised using the ABCD approach for finding the optimal distances for the desired magnification and the focus of the optical funnel. Schematically, the re-imaging setup is shown in Figure S.1 (c).

The parameters that describe the geometry of the re-imaged beam are expressed as follows [8]:

$$d_1 = \frac{(d_2 f_1 - f_1 f_2)d_3 - d_2 f_1 f_2}{(d_2 - f_1 - f_2)d_3 - d_2 f_2 + f_1 f_2} \tag{S.9}$$

$$M(d_3) = \frac{f_2(d_2 - f_1) - d_3(d_2 - f_1 - f_2)}{f_1 f_2} \tag{S.10}$$

$$\Theta = \arctan\left[\left(\frac{d_2 - f_1 - f_2}{f_1 f_2}\right) r_0\right] \tag{S.11}$$

Equation S.10 presents the magnification of the object's image depending on distance d_3, thus determining the radius of the optical funnel $r_0'(d_3) = M(d_3) r_0$. It should be noted that the imaging system must satisfy the condition $d_2 > f_1 + f_2$ in order to form a divergence Θ (Equation S.11) along the propagation. The main purpose of the optimisation stage via the de-magnifying system is to re-image the Bessel beam focus into the desired spot with chosen magnification, called from now on as the focus of the optical funnel.

The optimization procedure for the construction of optical funnels with parameters matching the experimental conditions begins taking a fixed d_2. Next, with the help of Equation S.5 and Equation S.10 we determine the desired magnification and, consequently, the focus size of the funnel. Finally, we calculate the distance where the object to be re-imaged should be located using the Equation S.9. There is a last variable that will help us in the characterization of the funnels, which is the divergence Θ of the optical funnel determined by Equation S.11.

S-II. FORMATION OF THE OPTICAL FUNNEL

The optical funnel was generated using a cw 532 nm Gaussian beam from a Coherent Verdi V5 diode-pumped laser. A 16-step spiral phase plate (Holo/Or, VL-204-Q-Y-A) of topological charge $l = 1$ produced a Laguerre Gaussian vortex beam with zero-intensity on the axis and a peak-to-peak diameter of the ring, $w_{pp} = 2.42$ mm. This beam was passed through an axicon with a wedge angle $\alpha_0 = 0.5°$ (Thorlabs AX2505-A) to produce a first-order Bessel beam of inner ring diameter $w_{pp} = 80\,\mu\text{m}$. The optical funnel beam was produced by re-imaging the quasi-Bessel beam inside the vacuum chamber using a 1:10 demagnifying collimator, composed of a plano-convex lens ($f_1 = 200$ mm) and a 10× long working distance microscope objective (Mitutoyo, $f_2 = 20$ mm). The optical funnel focus was formed 38 mm beyond the 10× objective, where $w_{pp} = 7.5\,\mu\text{m}$. The funnel extended ≈55 mm after the focus with a divergence of the central peak of ≈1.28 mrad. The method we used to map the profile of the optical funnel into the field of view of the camera is presented in Fig. S5. A laser beam stabilization system (MRC Systems) was integrated in the optical path, which actively corrected the beam pointing direction with high accuracy. This kept the pointing fluctuation of the optical funnel focus position in the chamber down to $\sigma_x = 84$ nm and $\sigma_y = 72$ nm, corresponding to a beam pointing stability below 4 µrad.

The diameter and propagation length of the optical funnel are controlled by the initial Gaussian beam diameter, the axicon geometry and refractive index, and the optical characteristics of the re-imaging collimator, namely the distance between the axicon and the collimator, the de-magnification rate, and the distance between the lenses in the collimator.

S-III. SAMPLE PREPARATION

Fluorescent polystyrene spheres of $2 \pm 0.08\ \mu$m diameter (density $\rho_{\text{PS}} = 1.05$ g/cm^3, FluoSpheres, Carboxylate-Modified Microspheres, yellow-green fluorescent) were used in these measurements. The samples were supplied as a 2 % solid fraction suspended in water plus 2 mM sodium azide, which were diluted to a concentration of roughly 1×10^8 particle/ml before the injection.

Granulovirus samples, which consist of individual viruses engulfed in crystallized protein occlusion bodies [9], were prepared as described previously [10]. Since the majority of the granulovirus particles consist of protein crystals, we assumed its density to be similar to that of a protein crystal, $\rho_{\text{GV}} = 1.4$ g/cm^3 [11], so the mass of a single virus is estimated as $2.2{\times}10^{-14}$ g. The sample was suspended in water to a concentration of roughly $5{\times}10^8$ particles/ml. An SEM image of Granulovirus particles is shown in Fig. S6.

S-IV. AEROSOL INJECTION

The particles were introduced into the gas phase by injecting them into a small nebulization chamber upstream of the injector using a gas dynamic virtual nozzle (GDVN) [12, 13] (see Figure 1). The GDVN produced liquid droplets with diameters of approximately 1–2 µm with sample flow rates in the range of 1–2 µL/ min. The flow rate of the GDVN helium sheath gas was in the range 10–40 mg/ min. The process of aerosol formation and transporting them into the injector is described in our previous work [14]. Located upstream of the injector was a nozzle/skimmer stage that was used to control the pressure in the injector. It consisted of an electropolished 300 μm ID nozzle and a 500 μm ID skimmer (Beam Dynamics, Inc.) with a 2–5 mm gap between them. The injector capillary (Swagelok #SS-6M0-R-2) had a 2 mm inner diameter (ID) and 12.5 mm length and was mounted at the end of a 4 mm ID tube of 300 mm length, inside the main chamber as shown in Figure 1. Excess gas was evacuated from the main chamber and skimmer stage with separate scroll pumps throttled by vacuum valves. The main particle-beam chamber and the GDVN nebulization chamber were $32 \times 32 \times 110$ mm^3 and $45 \times 45 \times 110$ mm^3 in volume, respectively (see Figure 1 in the main text).

S-V. PARTICLE IMAGING

Particles were imaged with two distinct imaging systems as shown in Figure 1. The first was a high-speed camera (Photron SA4) combined with a long working distance objective (Mitutoyo MY5X-802 – 5×) to provide a magnified field of view (FOV) of 2×2 mm^2. The second was a high quantum efficiency camera (photometrics prime 95B) combined with a variable-zoom objective (Thorlabs MVL6X12Z–6.5×) and was used to produce a lower magnification with larger FOV in the range of 4×4 mm^2 – 10×10 mm^2.

The illumination for both cameras was provided by either a side illuminating Nd:YLF laser (Spectra Physics Empower ICSHG-30, 527 nm, repetition rate 1 kHz, pulse duration 150 ns, pulse energy 20 mJ, average power 20 W) or an oblique-illuminating fiber-coupled diode laser (DILAS IS21.16-LC, 637 nm, 10–100 ns pulses, repetition rates up to 1 MHz, average power 10 W). The output of the Nd:YLF laser was focused by a cylindrical lens of focal length 75 mm to form a light-sheet of size 5 mm × 20 μm parallel to and intersecting the axis of the particle beam as shown in Figure 1. The intense and short pulse duration of the Nd:YLF laser produced single snapshots of many particles without significant motion blur. However, due to the relatively slow repetition rate of this illumination, images of individual particles were recorded at most once in a single frame. Therefore, such particle images were used to count particles passing through the FOV in a given time and reconstruct the two-dimensional particle density map, as discussed in section S-VI below. These particle positions were accumulated over a number of frames to reconstruct the two-dimensional particle density map, which represents an instantaneous average particle number density.

The output from the fiber-coupled diode laser was collimated and focused into the chamber using a fiber output collimator (Thorlabs F810SMA-635) and a plano convex lens, $f = 50$ mm. Typically, the diode laser was operated at a repetition rate between 25 kHz and 100 kHz, whereas the camera recorded frames at 1 kHz and 1 ms exposure. Therefore, using this illumination, a single particle could be imaged multiple times in a single frame, as depicted in figure Figure 3 (a). Since the centroids of the images of particles could be accurately determined from the frames, and the time between each snapshot was accurately known, such images could be used to extract the particle trajectories and study the particle dynamics, as discussed in S-VI Section below. Importantly, due to the broad range of particle speeds and resulting overlaps in the slower-moving particle images, it was not possible to quantitatively track all particle trajectories at a laser pulses repetition rate of 25 kHz when the optical funnel was turned on.

S-VI. DATA ANALYSIS

Background noise in the particle images hampers their analysis and thus must be kept to a minimum. We found that the main source of noise in the recorded data was light scattered from the stainless steel injector tip and the chamber walls. Most of the background arising from the optical funnel was blocked by the optical filters shown in Figure 1, whereas the relatively constant background produced by the illumination lasers was reduced by subtracting a time-integrated median background image from every raw frame. This was followed by a spatial band-pass filtering of the images to smooth them and eliminate the remaining high frequency background.

After the pre-processing of images, particles were identified by searching for connected pixels with intensities and size above an empirically determined threshold. Intensity centroids were then calculated for each group of connected pixels for every frame, and stored as list of coordinates. For particle number density determination, centroid positions were extracted from images collected over a period of time. These positions were accumulated into the two-dimensional particle density profile as shown in Figure 4 (a,b) in the main text. To better represent the particle density improvement by the introduction of the optical funnel we typically normalize the laser on and the laser-off 2D particle beam profiles by the maximum particle beam density measured in the laser-off. Note that in these measurements the particles were illuminated by the Nd:YLF laser.

For velocity and acceleration analysis, first the particle trajectories must be extracted from each frame of the analysed centroid data set. This was done by searching for clusters of particle centroids in a frame which belong to the same particle trajectory, using a density-based spatial clustering of applications with noise (DBSCAN) clustering algorithm [15]. Particle velocities and accelerations were then determined from each found trajectory, using finite difference calculations based on the known illumination laser frequency, as shown in Figure 3 (c-e). This characterisation of the particle dynamics can be used to calculate the forces and light-induced temperature changes on the particles, as discussed in the next Section. The analysis was done using a custom Matlab script.

S-VII. ESTIMATION OF FORCES AND TEMPERATURE GRADIENTS

We estimate the temperature gradient across the granulovirus particles by comparing our measured forces to the expression relating the photophoretic force to the temperature gradient across a spherical particle in the high-Knudsen-number regime. The granulovirus particles have a size of approximately 265 × 265 × 445 nm^3 [9] which is equivalent to the volume of a sphere with radius $r = 162$ nm and a mass of $m = 2.2 \times 10^{-14}$ g. The Knudsen number $\mathrm{Kn} = 1320$ is defined here as the ratio of the mean-free-path of the gas to the particle radius. The mean-free-path $\lambda = 429$ μm for helium may be calculated by the formula

$$\lambda = \frac{kT}{2\sqrt{\pi} P d_m^2} \tag{S.12}$$

where k is the Boltzmann constant, $T = 298$ K is the gas temperature, $P = 40$ Pa is the gas pressure, and $d_m = 260$ pm is the kinetic diameter of helium. The photophoretic force is derived from the gas kinetic theory[16, 17] and described by the following equation:

$$F^{pp} = \frac{\pi}{6}\alpha P r^2 \frac{\Delta T}{T} \tag{S.13}$$

where $\alpha \approx 1$ is the thermal accommodation coefficient of the particle, and ΔT is the temperature difference across the particle. The equation of motion of a particle relates acceleration to the combined photophoretic forces ($\vec{F}^{pp}$), optical scattering and absorption forces ($\vec{F}^{opt}$), and gas drag force ($\vec{F}^{d}$). Assuming a symmetric optical beam, we expect two relevant force components for a particle in the x–z plane:

$$\begin{cases} ma_x = F_x^{pp} + F_x^{opt} + F_x^{d} \\ ma_z = F_z^{pp} + F_z^{opt} + F_z^{d} \end{cases} \tag{S.14}$$

where the subscripts x and z refer to the transverse and axial components, respectively. The slip-corrected drag force $\vec{F}^{d}$ for a particle in the high-Kn regime is

$$\begin{aligned} \vec{F}^{d} &= \frac{6\pi\mu r(\vec{v}_g - \vec{v}_p)}{C} \\ C &= 1 + \mathrm{Kn}(c_1 + c_2 \cdot e^{\frac{-c_3}{\mathrm{Kn}}}), \end{aligned} \tag{S.15}$$

where C is the Cunningham slip-correction factor, introduced by Knudsen and Weber, with empirical coefficient of, $c_1 = 1.231$, $c_2 = 0.4695$ and $c_3 = 1.1783$ [18, 19]. v_p and v_g are the velocity of the particle and the gas, respectively.

In order to understand the importance of gas drag forces, we numerically simulated the gas velocity using the injector geometry and the measured pressures upstream and downstream of the injector as an input. The Navier–Stokes equations were solved with a finite-element solver using the COMSOL Multiphysics software suite [18]. As shown in figure Figure S.2, close to the exit of the injector the gas expands with relatively high velocity, which also accelerates the particles. However, below 15 mm from the the injector, where our measurements were performed, the gas decelerates to negligible velocity. Under the assumption of negligible gas velocity, Equation S.15 predicts a deceleration of approximately 2.2×10^4 m/s^2 for granulovirus particles in absence of laser illumination at the typical measured speed 17.5 m/s. This predicted value is not far from our measured acceleration of 1.42×10^4 m/s^2, which we obtained from the acceleration/velocity histograms shown in Figure S.3. These histograms moreover reveal a relatively small acceleration of $a_z = 43$ m/s^2 at zero velocity. Based on these calculations and observations, we assume the gas velocity to be zero in subsequent calculations.

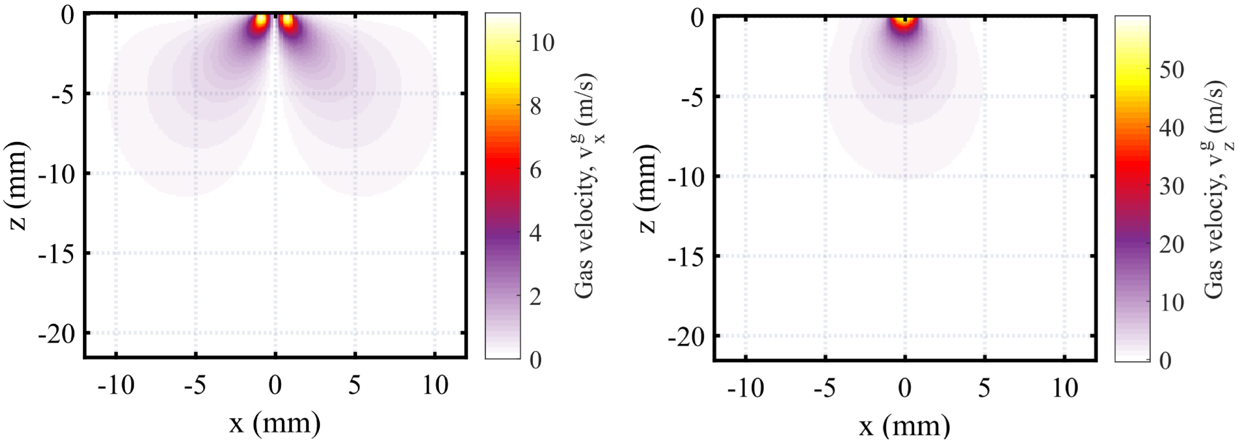

(a)

(b)

FIG. S.2. The simulated He gas velocity between the exit of the aerosol injector and optical funnel focus at 0.99 mbar chamber pressure.(a) The velocity along the transverse direction and (b) the velocity along the axial direction. The injector exit is at $z = 0$. This simulations were performed as described in our previous publication [18].

We now consider the particle trajectory shown in main text Figure 3, in which the peak acceleration at the time $t = 0.15$ ms is 9.6×10^3 m/s^2 at a particle speed of 2.2 m/s. At 0.99 mbar, the mean-free-path of helium gas is 172 µm, and Knudsen number, Kn = 528, the relevant measurement parameters are listed in Table S.2. After subtracting the slip-corrected drag force, the combined photophoretic and optical force is 6.2×10^{-14} N, which suggests that the photophoretic force is dominant since the maximum possible radiation pressure is $F_z^{opt} \approx \pi r^2 I/c \approx 8.3 \times 10^{-14}$ N at the peak intensity in the optical funnel ($I = 3.0 \times 10^8$ W/m^2). Thus the peak acceleration suggests that $\Delta T/T = 0.045$, and $\Delta T \geq 13.4$ K since $T \geq 298$ K. If we assume the thermal conductivity of granulovirus to be $g = 0.3$ W/m/K (comparable to most polymers and protein-based materials) then the approximate intensity of thermal energy transferred across the granulovirus at this temperature difference is of order $I_{\text{heat}} \approx g\Delta T/r \approx 2.47 \times 10^7$ W/m^2.

S-VIII. POSITIONING OF THE OPTICAL FUNNEL IN THE CAMERA FOV

To map the location of the optical funnel in the camera FOV we rely on Rayleigh scattering imaging of high density particles illuminated by the optical funnel. In these measurements,

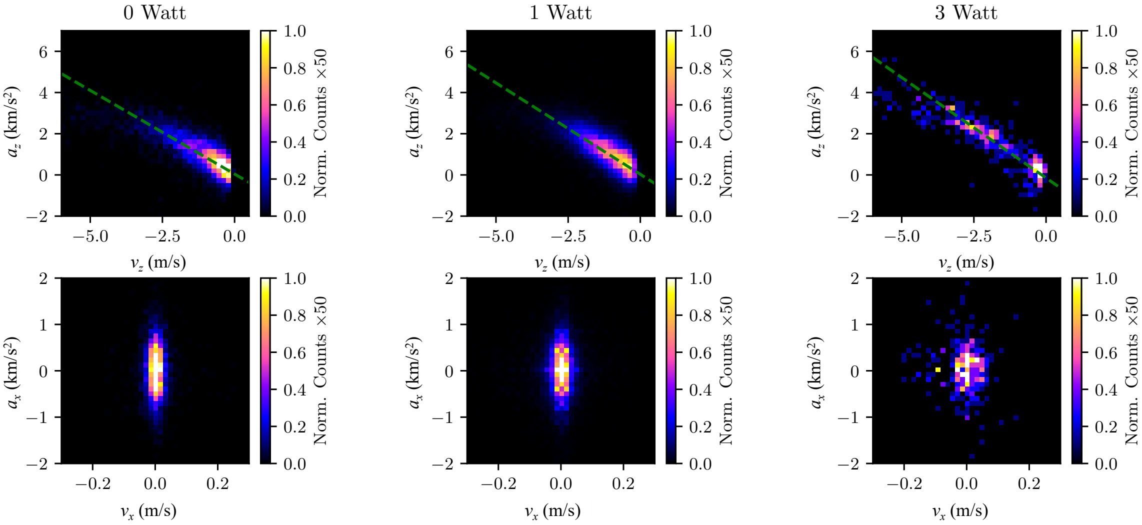

FIG. S.3. Granulovirus velocities and accelerations under different optical funnel illumination conditions, each at 0.99 mbar pressure (see Table S.2 for experimental parameters). Histograms of particle acceleration and velocity for the z and x axes are shown in the top and bottom rows, respectively, with columns corresponding to 0, 1 and 3 Watt optical funnel powers, respectively. The velocities and accelerations were estimated from finite differences in centroid positions using triplets of sequential images determined from 25 kHz stroboscopic images. The green dashed line in the middle row corresponds to a linear fit to the function $a_z = av_z + b$. The resulting values for the $\{0, 1, 3\}$-Watt optical funnel illumination were $a = \{-810, -890, -980\}$ s^{-1} and $b = \{0.043, 0.030, -0.15\}$ km/s^2.

the optical funnel was propagating opposite to the particles and the scattered intensity was recorded on the camera which was set to a relatively long exposure time of 20 ms. This produce long streak-images of the particles, similar to streak-imaging described in [20]. These images were pre-processed to remove the background and the scattered image intensities were integrated through the measured frames. Then the beam profile is reconstructed by pixel by pixel weighted averaging of this integrated image intensity.

Figure S.5 (a) shows the two dimensional reconstructed optical funnel profile generated from the 5000 frames each containing streaked scattering intensity of granulovirus particles

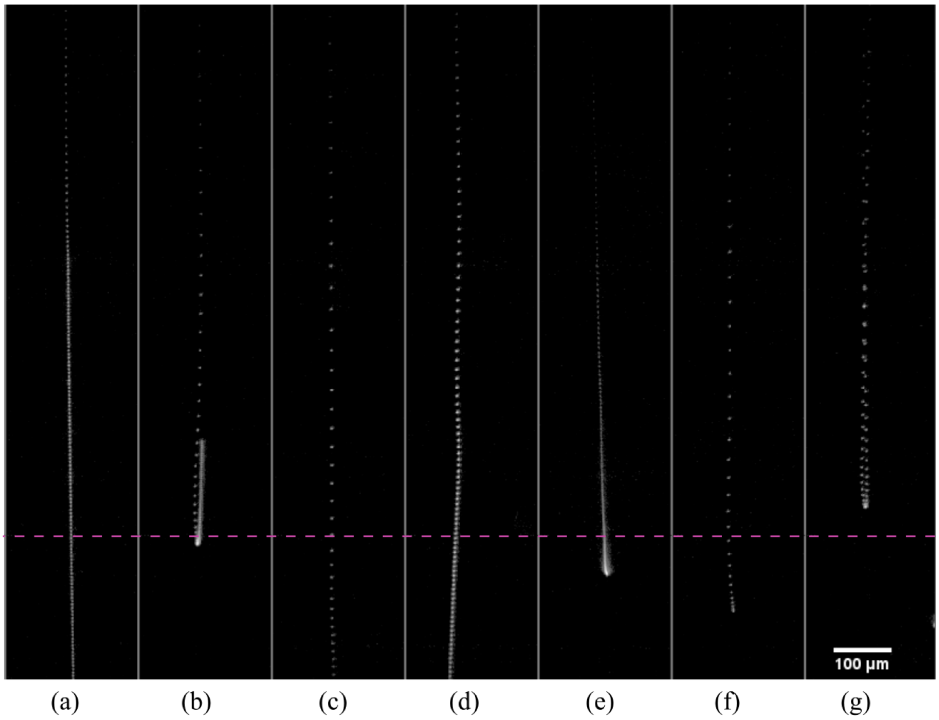

FIG. S.4. Selected background corrected stroboscopic images of 2 micrometer diameter polystyrene particles trajectories in 5 W optical funnel. This measurement was performed at 1.5 mbar chamber pressure and the particles were illuminated by the DILAS laser operating at 100 kHz. In this images, the optical funnel was propagating in the vertical direction and the horizontal dashed-line indicates the position of focal plane in the images, how we determined this position is shown in Figure S.5.

illuminated by a 0.2 watt optical funnel. The axial cross-section of the beam is shown in Figure S.5 (b). The maximum intensity position, indicated by the green dashed line, shows the focus of the optical funnel. This position is used to define the center of our coordinate system. Similarly, the beam position can also be inferred by time integrating air scattering intensity in the optical funnel path as seen in Figure S.5 (c). Using these techniques, we can determine the focal position of the optical funnel with a resolution better than a micrometer.

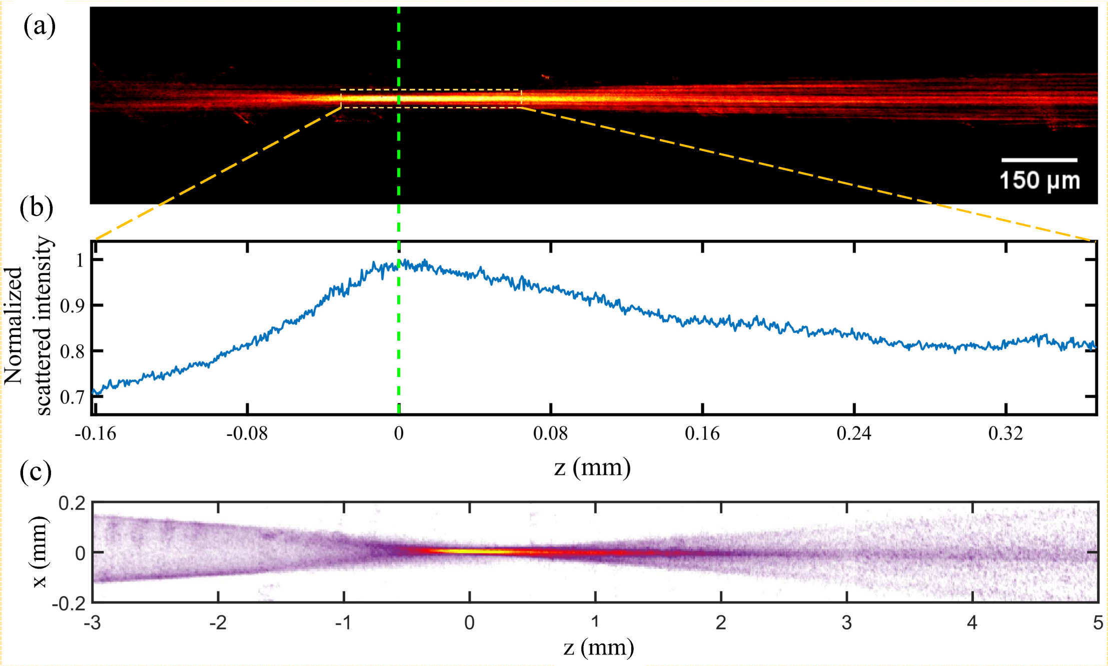

FIG. S.5. Mapping the optical funnel in the camera FOV using particles or air scattering intensities. (a) The reconstructed two dimensional intensity profile of the optical funnel. This profile is generated by integrating 5000 frames, each containing long exposure scatted intensity of GV particles illuminated by a 0.2 watt optical funnel. (b) Normalized axial cross-section of the intensity profile in (a). The green dashed-line indicates the focal plane of the optical funnel. (c) The optical funnel profile generated by time integrating air scattering in the beam path.

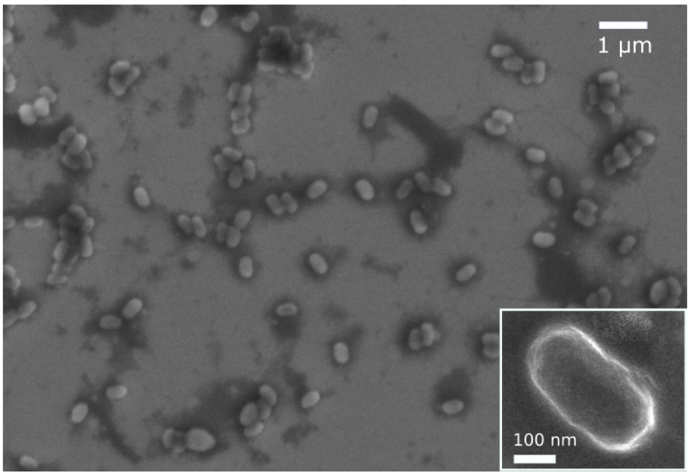

FIG. S.6. Scanning electron microscope image of granulovirus particles suspended on silicon substrate.

S-IX. EXPERIMENTAL PARAMETERS

	granulovirus	**2 μm polystyrene**
Mean particle velocity, V_z, with laser-off (m/s)	17.4 ± 0.93	12.87 ± 0.97
Optical funnel power (W)	0, 0.5	0, 2.5, 5.0
Chamber pressure (mbar)	0.4	0.5
Sample concentration (particles/ml)	$5{\times}10^8$	$7.5{\times}10^7$
Particle generation rate (particles/second)	1.17×10^4	2.25×10^3
GDVN gas flow rate	15 mg/min	16 mg/min

TABLE S.1. Experimental parameters for the particle beam focusing presented in Figure 4.

	granulovirus
Mean particle velocity, V_z, with laser-off (m/s)	-1.72± 0.42
Optical funnel power (W)	0, 1.0, 3.0
Chamber pressure (mbar)	0.99
Sample concentration (particles/ml)	$5{\times}10^8$
Particle generation rate (particles/second)	2.18×10^4
GDVN gas flow rate	14 mg/min

TABLE S.2. Experimental parameters for the granulovirus particle dynamics presented in Figure 3 and Figure S.3.

REFERENCES

[1] B. E. Salehand M. C. Teich, *Fundamentals of photonics* (Wiley-Interscience, New Jersey, 2007).

[2] R. W. Bowmanand M. J. Padgett, Optical trapping and binding, Rep. Prog. Phys. **76**, 026401 (2013).

[3] J. H. McLeod, The axicon: A new type of optical element, J. Opt. Soc. Am. **44**, 592 (1954).

[4] N. Eckerskorn, R. Bowman, R. A. Kirian, S. Awel, M. Wiedorn, J. Küpper, M. J. Padgett, H. N. Chapman, and A. V. Rode, Evaluation of optically induced forces imposed in an optical funnel on a stream of particles in air and in vacuum, Phys. Rev. Appl. **4**, 064001 (2015).

[5] N. Eckerskorn, L. Li, R. A. Kirian, J. Küpper, D. P. DePonte, W. Krolikowski, W. M. Lee, H. N. Chapman, and A. V. Rode, Hollow Bessel-like beam as an optical guide for a stream of microscopic particles, Opt. Express **21**, 30492 (2013).

[6] O. Brzobohatý, T. Čižmár, and P. Zemánek, High quality quasi-bessel beam generated by round-tip axicon, Opt. Express **16**, 12688 (2008).

[7] V. Jarutis, R. Paškauskas, and A. Stabinis, Focusing of Laguerre-Gaussian beams by axicon, Opt. Commun. **184**, 105 (2000).

[8] S. Lavin-Varela, M. Ploschner, and A. Rode, Developing a needle-like optical funnel: numerical modelling, in *Optical Trapping and Optical Micromanipulation XVI*, Vol. 11083, edited by K. Dholakiaand G. C. Spalding, International Society for Optics and Photonics (SPIE, 2019) pp. 244 – 254.

[9] C. Gati, D. Oberthuer, O. Yefanov, R. D. Bunker, F. Stellato, E. Chiu, S.-M. Yeh, A. Aquila, S. Basu, R. Bean, K. R. Beyerlein, S. Botha, S. Boutet, D. P. DePonte, R. B. Doak, R. Fromme, L. Galli, I. Grotjohann, D. R. James, C. Kupitz, L. Lomb, M. Messerschmidt, K. Nass, K. Rendek, R. L. Shoeman, D. Wang, U. Weierstall, T. A. White, G. J. Williams, N. A. Zatsepin, P. Fromme, J. C. H. Spence, K. N. Goldie, J. A. Jehle, P. Metcalf, A. Barty, and H. N. Chapman, Atomic structure of granulin determined from native nanocrystalline granulovirus using an x-ray free-electron laser, Proc. Natl. Acad. Sci. U.S.A. **114**, 2247 (2017).

[10] D. Oberthür, J. Knoska, M. Wiedorn, K. Beyerlein, D. Bushnell, E. Kovaleva, M. Heymann, L. Gumprecht, R. Kirian, A. Barty, V. Mariani, A. Tolstikova, T. White, L. Adriano, S. Awel, M. Barthelmes, K. Dörner, L. X. Paulraj, O. Yefanov, D. James, J. Chen, G. Nelson, D. Wang,

A. Echelmeier, B. Abdallah, A. Ros, G. Calvey, Y. Chen, S. Frielingsdorf, O. Lenz, A. Schmidt, M. Szczepek, E. Snell, P. Robinson, Božidararler, G. Belsak, M. Macek, F. Wilde, A. Aquila, S. Boutet, M. Liang, M. Hunter, P. Scheerer, J. D. Libscomb, U. Weierstall, R. Kornberg, J. Spence, L. Pollack, H. N. Chapman, and S. Bajt, Double-flow focused liquid injector for efficient serial femtosecond crystallography, Sci. Rep. **7**, 44628 (2017).

[11] M. L. Quillinand B. W. Matthews, Accurate calculation of the density of proteins, Acta Cryst. D **56**, 791 (2000).

[12] D. P. DePonte, U. Weierstall, K. Schmidt, J. Warner, D. Starodub, J. C. H. Spence, and R. B. Doak, Gas dynamic virtual nozzle for generation of microscopic droplet streams, J. Phys. D **41**, 195505 (2008).

[13] K. R. Beyerlein, L. Adriano, M. Heymann, R. Kirian, J. Knoska, F. Wilde, H. N. Chapman, and S. Bajt, Ceramic micro-injection molded nozzles for serial femtosecond crystallography sample delivery, Rev. Sci. Instrum. **86**, 125104 (2015).

[14] S. Awel, R. A. Kirian, M. O. Wiedorn, K. R. Beyerlein, N. Roth, D. A. Horke, D. Oberthür, J. Knoska, V. Mariani, A. Morgan, L. Adriano, A. Tolstikova, P. L. Xavier, O. Yefanov, A. Aquila, A. Barty, S. Roy-Chowdhury, M. S. Hunter, D. James, J. S. Robinson, U. Weierstall, A. V. Rode, S. Bajt, J. Küpper, and H. N. Chapman, Femtosecond X-ray diffraction from an aerosolized beam of protein nanocrystals, J. Appl. Cryst. **51**, 133 (2018), arXiv:1702.04014.

[15] M. Ester, H.-P. Kriegel, J. Sander, X. Xu, *et al.*, A density-based algorithm for discovering clusters in large spatial databases with noise., in *KDD-96: Proceedings of the Second International Conference on Knowledge Discovery and Data Mining*, Vol. 96 (1996) pp. 226–231.

[16] H. Rohatschek, Semi-empirical model of photophoretic forces for the entire range of pressures, J. Aerosol Sci. **26**, 717 (1995).

[17] H. Horvath, Photophoresis – a forgotten force ??, KONA Powder and Particle Journal **31**, 181 (2014).

[18] N. Roth, S. Awel, D. A. Horke, and J. Küpper, Optimizing aerodynamic lenses for single-particle imaging, J. Aerosol Sci. **124**, 17 (2018), arXiv:1712.01795 [physics].

[19] D. K. Hutchins, M. H. Harper, and R. L. Felder, Slip correction measurements for solid spherical particles by modulated dynamic light scattering, Aerosol Sci. Techn. **22**, 202 (1995).

[20] S. Awel, R. A. Kirian, N. Eckerskorn, M. Wiedorn, D. A. Horke, A. V. Rode, J. Küpper, and

H. N. Chapman, Visualizing aerosol-particle injection for diffractive-imaging experiments, Opt. Express **24**, 6507 (2016).